Impedance analysis for methane and CO_2 discrimination in coalbeds

Diane J. Lespinasse, Christopher R. Clarkson, Robert J. Ferguson

ABSTRACT

In this paper, we present a methodology to evaluate the use of Elastic Impedance and Elastic Impedance Coefficient to discriminate coals saturated with methane from coals saturated with CO_2. We apply this methodology to a dataset of the Fruitland coals Fairway, in the North of the San Juan Basin U.S, which is considered the most productive reservoir of Coalbed methane in the world.

In this project, we develop a proxy model of a 15.25m (50ft) coalbed at a depth of 914.4m (3000ft) over an area of 31.4km^2. We obtain the production forecast of 24 wells during primary production and during enhanced coalbed methane by CO_2 injection, starting in 1999 and continuing until 2031. Based on the results of the fluid simulation, we perform a Gassmann fluid substitution to model the variation in Vp, Vs and density due to the changes of fluid saturations in the pore space, assuming 100% of brine saturation as the initial state. In this paper we present three cases: the area after several years of depletion, after two years of CO_2 injection, and one year after shutting the injector wells. As a result, we observe that the most representative changes are associated with V_p, which presents a decrease of 55-65m/s after shutting the injector wells.

As a final step, we estimate Elastic Impedance and the Elastic Impedance Coefficient. In the case of Elastic Impedance we observe a decrease in the zones around the injector wells that were associated with the movement of the CO_2 flood. The Elastic Impedance Coefficient tends to increase around the injector wells, showing the movement of the CO_2 front; and it seems to highlight better the effects of CO_2 injection. It was not possible to use EI and EC to discriminate CO_2 from methane in this study since the values associated to the areas saturated with CO_2 coincides with the values associated to some areas saturated with methane. The magnitude of the changes of EI and EC are small and it is difficult to predict whether the changes will be appreciated in seismic data.

INTRODUCTION

Lately, the coalbed methane industry has been growing and important advances in exploration, production and the development of technology have been achieved (Jenkins et al., 2008). Thanks to these advances, coalbed methane has become an important source of natural gas and studies that aim to determine the physical properties of coals and monitor coalbed methane primary and enhance production are increasingly important. Koperna and Oudinot (2009) discuss different methods of monitoring, verification and accounting of the displacement of CO_2 injected in a coalbed; and Lespinasse and Ferguson (2010), evaluate the seismic response of the Mannville coals in the Corbett Field, Alberta, Canada during primary production and also perform a sensitivity test to establish resolution limits by applying a methodology previously develop by Zarantonello et al. (2010).

In this project, we attempt to discriminate coals saturated with methane from coals saturated with CO_2 by estimating Elastic Impedance and the Elastic Impedance Coefficient. We also evaluate the possibility of monitoring the movement of the CO_2 flood by using these attributes.

This paper begins with a brief introduction to the concepts of Elastic Impedance and Elastic Impedance Coefficient and their use for lithology and fluid discrimination. Then, we describe the methodology applied during the development of this project, including the fluid simulation, data selection, estimation of the fluid properties using Batzel and Wang (1992) equations, and the Gassmann Fluid substitution. We then present details of the data used in this project and the procedure that we follow to perform all the calculations involved. Finally we present the results of the fluid simulation, the Gassmann fluid substitution and the estimation of the Elastic Impedance and the Elastic Impedance Coefficient for three stages of primary and enhanced production: after several years of depletion (primary production), after two years of enhanced production by CO_2 injection, and one year after stopping injection.

THEORETICAL DEVELOPMENT

Elastic Impedance

The concept of Elastic Impedance (EI) begins with the development provided by Whitcombe (2002) as a tool that was initially used for the fluid evaluation in the Shetlands Foinaven Field (Whitcombe et al., 2002). Connolly (1999) defined Elastic Impedance (EI) as an analogue of the Acoustic Impedance (AI) that takes into account the variation of the incidence angle, and its derivation is based on the Aki and Richards (1980) linearization for the Zoeppritz equation (Whitcombe, 2002).

Elastic Impedance is a function that relates the compressional wave velocity (V_p), the shear wave velocity (V_s), and the density, as shown in equation 1:

$$EI = V_p^{(1+tan^2\theta)} V_s^{(-8Ksin^2\theta)} \rho^{(1-4Ksin^2\theta)} \quad (1)$$

where θ is the incidence angle (Connolly, 1999) and K is defined as a constant over the section of interest, and it is estimated as the mean value of $(V_s/V_p)^2$. From equation 1, it is established that for an incidence angle $\theta=0$, the Elastic Impedance will be equal to the Acoustic Impedance (Whitcombe, 2002).

Connolly (1999) presents Elastic Impedance as a tool to perform calibration of far offset seismic data. In this order, synthetic seismograms in terms of the incidence angle can be generated for calibration or inversion purposes (Connolly, 1999).

An important application of the Elastic impedance is that it can be used to perform a preliminary evaluation of the amplitude versus offset (AVO) response in an efficient and time effective way. Also, the changes in Elastic Impedance can be evaluated to determine a correlation with any rock property that allows us to achieve; for example, lithology or fluid discrimination (Connolly, 1999).

In 2008, Cao et al. introduced the concept of the Elastic Impedance Coefficient (EC) as relationship proportional to the Acoustic Impedance and inversely proportional to Elastic Impedance (equation 2).

$$EC = \frac{AI}{EI} \tag{2}$$

where AI is the Acoustic Impedance and EI is the Elastic Impedance.

The Elastic Impedance Coefficient establishes a combination of the Acoustic Impedance and Elastic Impedance to create a stronger attribute for lithology, and fluid discrimination; and gas saturation estimation. Cao et al (2008), provide some examples in which the Elastic Impedance Coefficient produced better results for lithology discrimination and the detection of the presence of gas than the Acoustic Impedance and the Elastic Impedance by themselves (Cao et al., 2008).

AREA OF STUDY

For the development of this study we used data that corresponds to the coalbeds of the Fruitland Formation, more specifically in the Coal Fairway located in the North part of the San Juan Basin.

The San Juan Basin is located in the western part of the United States of America and extends through the South West of Colorado and the North West New Mexico State (Magill et al., 2010), covering an area of approximately 38000km^2 (Laubach and Tremain, 1991).

The structure of the San Juan Basin was defined by the Laramide Orogeny between the Late Cretaceous and the Eocene (Kaiser and Ayers, 1994) which caused the generation of folds and faults along the boundaries of the basin. The San Juan Basin is interpreted as an asymmetrical syncline having its axis in the South border of Colorado State. The limits of the San Juan Basin are determined by the Hogback Monocline to the North, the Defiance Monocline to the South West and the Zuni Uplift to the South (Crist et al., 1989). Figure 1a shows the extension and limits of the San Juan Basin.

The San Juan Basin presents sediment fill of continental and marine origin, deposited during the Cretaceous and the early Tertiary (Laubach and Tremain, 1991) and they are associated with cycles of transgresive-regresive deposition. The dominant lithologies in this basin are shale, siltstone and sandstone with a less significant presence of coal and limestone (Michael et al., 1993). The natural gas production from Fruitland coal in the San Juan Basin started in 1986 (Magill et al., 2010), and since that moment it has become a significant source of natural gas for the U.S.

Fruitland Formation

The deposition of the Fruitland Formation occurred in the Late Cretaceous (Snyder et al., 2003) and it is mainly compose of shale, siltstone, sandstone and coal. The deposition of this Formation is associated with one of the regressive cycles that took place in the San Juan Basin (Michael et al., 1993) and can be interpreted as occurring over a 7 million year period (Pashin, 1998).

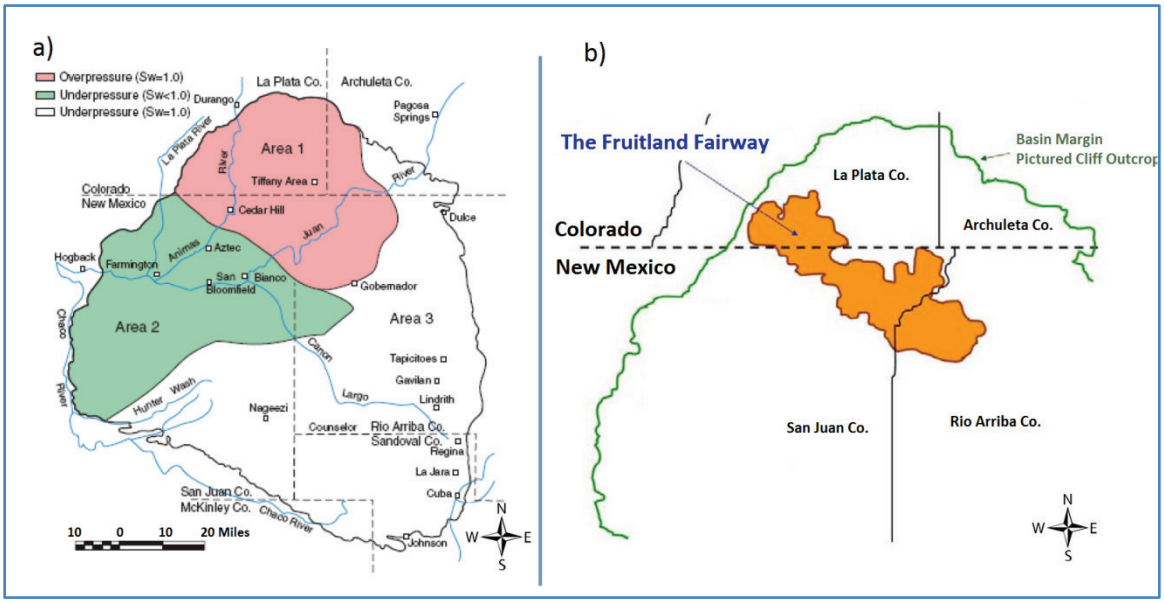

FIG. 1. a) San Juan Basin map (Figure 1, Magill et al., 2010) and b) Fruitland coals Fairway (Figure 1, Ramurthy and Lyons, 2007)

The Lewis Shale and the Pictured Cliffs Sandstone Formations underlie the Fruitland Formation. These Formations were deposited in an open marine and a shoreface environment respectively, and are associated with a highstand system track. Lewis Shale and the Picture Cliffs Formations present sediments, which become coarser to the upward direction, and have a thickness of approximately 400m (Pashin, 1998). A retreat of the sea during the Late Cretaceous, led to the deposition of coastal sediments that form the Fruitland Formation (Snyder et al., 2003) (Laubach and Tremain, 1991). Conformably, the sandstones and shales that form the Kirtland Shale Formation were deposited overlying the Fruitland Formation. Having a thickness of approximately 200m (Pashin, 1998), the Kirtland Shale has been interpreted as a regional seal (Oudinot et al., 2009).

Figure 2 shows a stratigraphic column of the Cedar hill field in the San Juan Basin.

The Fruitland Formation has a maximum thickness of approximately 150m (Michael et al., 1993). It presents its thicker part in the NW area of the San Juan Basin and it becomes thinner and disappears towards the East (Laubach and Tremain, 1991). Laterally discontinuous coalbeds of up to 12m thickness constitute the Fruitland Formation (Michael et al., 1993) with approximately 30m of coal total net thickness (Jenkins et al., 2008).

The maceral content of Fruitland coals is mostly vitrinite which constitutes approximately 80% of the total macerals; the 20% left corresponds to exinite and inertinite (Michael et al., 1993). Coals from the Fruitland Formation have an ash content of approximately 8-30% (Laubach and Tremain, 1991) with a rank that increases from sub-bituminous to bitouminous (low volatile) towards the north direction (Jones, 2003).

The Fruitland coals have cleat porosity between 0.5-2% (Snyder et al., 2003) and in some cases minerals like pyrite, calcite and gypsum partially fill them. The face cleats,

which formed earlier than the butt cleats, are well developed and have an extension on the order of meters. The butt cleats have an extension of 10cm or less and show an intersection angle of 80-90° with the face cleats (Laubach and Tremain, 1991).

In the north of the San Juan Basin, there is an area called the Fruitland coals Fairway (Magill et al., 2010) with an extension that corresponds to 15% of the coalbed methane productive zones in the basin. The coal Fairway is an over-pressured area characterized by the presence of thicker coalbeds in the Fruitland Formation (Jenkins et al., 2008), with higher coal rank, lower ash content, better developed cleat systems (Magill et al., 2010) and higher permeability in the range of 20-100mD. The Coal Fairway is recognized by being the most productive reservoir of coalbed methane in the world and is responsible of approximately 75% of the coalbed methane produced from the San Juan Basin (Jenkins et al., 2008). Figure 1b presents the Fairway location in the San Juan Basin.

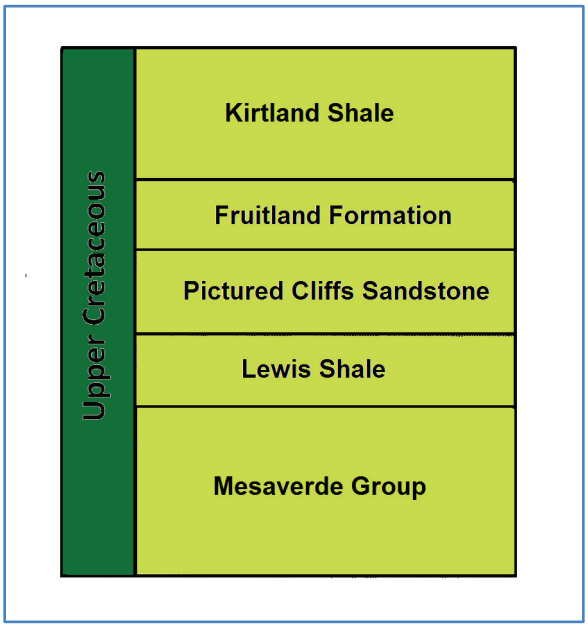

FIG. 2. Stratigraphic column of the San Juan Basin (Modified from Figure 2, Young et al., 1991)

METHODOLOGY

Fluid simulation

Geological data and production data from the Fruitland coals was collected to develop a proxy model of the Fruitland Coal Fairway in the San Juan Basin.

Initially, a vertical single well model was built and dynamic data was included. For this model, the history match was performed using production data from this well. This single well model allowed us to evaluate the relative permeability and relative adsorption data that was being used.

Based on this single well model a field model was built. The reservoir model was developed with a grid dimension of 175x175x1, with producing wells on 320-acre

spacing. For this project, a single coalbed layer with a thickness of 15.24m (50ft) at a depth of 914.4m (3000ft) was modeled over an extension of 31.4 km^2.

The inputs for the generation of the reservoir model were:

- Historical gas production and water production
- Relative permeability curve associated to the Fairway area
- Langmuir isotherms for CO_2 and methane
- A function that determines the absolute permeability growth in terms of reservoir pressure
- Relative adsorption data for CO_2 and methane calculated with the Extended Langmuir model.

Langmuir parameters are presented in Table 1 and Table 2 shows the model assumptions.

Table 1. Lagmuir parameters

Langmuir Parameters	
Langmuir Volume V_L CH_4	472 scf/ton
Langmuir Pressure P_L CH_4	592.2 psia
Langmuir Volume V_L CO_2	689scf/ton
Langmuir Pressure P_L CO_2	259.3 psia

Table 2. Reservoir model assumptions

Model assumptions	
Coal thickness	15.24m (50ft)
Top of the coalbed	914.4m (3000ft)
Grid size	175x175x1
Area of study	31.4km^2
Absolute permeability	80mD
Initial pressure	1616psia
Temperature	41.66 ^oC
Fracture porosity	0.0035 (fraction)
Initial water saturation	100%
Skin	0

Using the reservoir model, the production forecast of primary depletion for 24 wells in the area of study was performed. The production forecast started in 1999 and extends until 2031.

This model was also used to forecast enhaced coalbed methane production by CO_2 injection. In this case, 4 CO_2 injection wells were added to the model. It was assumed that the injection started in July 2003 and was shut in October 2010 and the forecast continuous until 2031.

Data selection

The compressional wave velocity V_p, the Shear wave velocity V_s and density values needed to perform the fluid substitution were selected from well log data available for different fields in the San Juan Basin.

The selection of V_p was based on an average of the slowness associated with coals, observed on the sonic log of the Glover Well, located in the Archuleta County in the San Juan Basin (Figure 3a). For the selection of V_p, we also used a velocity model generated for the Hamilton 3 well, which was based in a sonic log that was run in this well (Figure 3b). Averages of the velocities associated with the upper and lower coalbed were taken into account.

The V_s velocity used in this study for the fluid substitution was selected by doing an average of the shear velocities associated to coals form the velocity model of the Hamilton 3 well (Figure 3b)

In the case of the density, we use an average of the coal densities obtained from bulk density logs of 4 wells located in Pump Canyon, inside the Fairway in the San Juan Basin (Figure 4)

Table 3 present the values of V_p, V_s and density used in this study to perform the fluid substitution.

Table 3. V_p, V_s and density values selected for the development of this study

Parameters for fluid substitution	
V_p	2450m/s
V_s	1025m/s
Density	1.6 g/cm^3

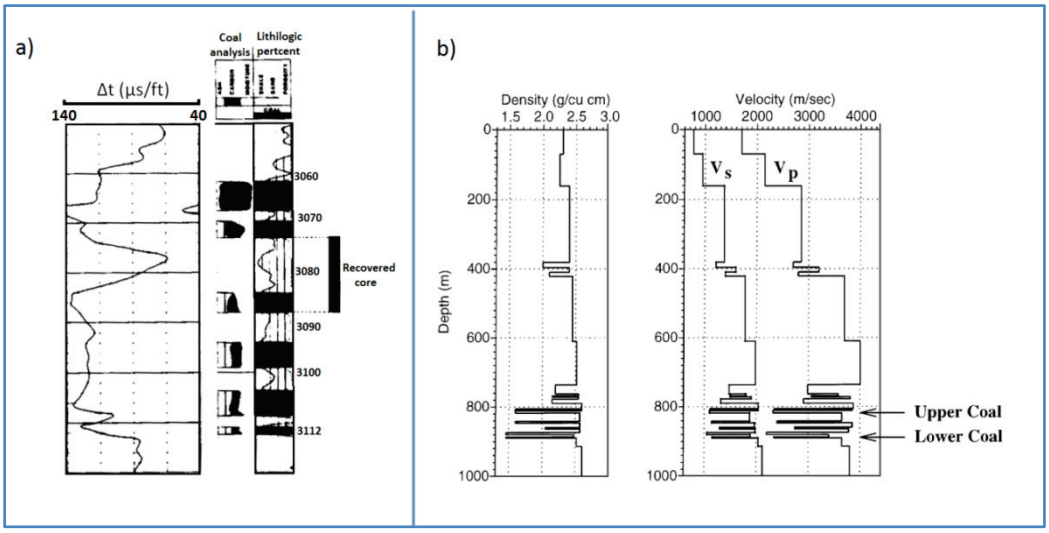

FIG. 3. a) Sonic log of Glover Well 1. Archuleta County, San Juan Basin (Modified from Figure 6, Jones et al., 1984) and b) V_p, V_s and density model from the Hamilton 3 well, Cedar Hill, San Juan Basin. (Figure 8, Ramos and Davis, 1997)

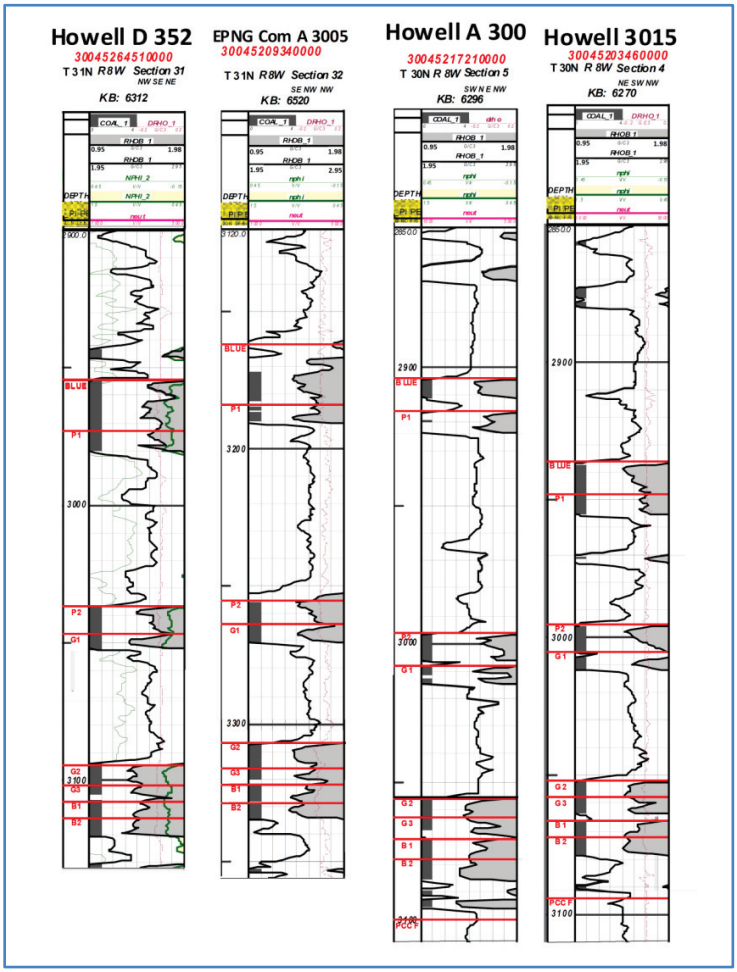

FIG. 4. Density logs. Pump Canyon, San Juan Basin (Modified from Figure 5, Koperna et al., 2009)

Fluid properties

We estimate the fluid properties, used for the Gassmann fluid substitution, with the equations presented by Batzel and Wang (1992). They use a series of relations, based on thermodynamic laws and empirical results, to make an approximation of density, bulk modulus, velocity and viscosity of the fluids and evaluate the dependence of these properties with the temperature, pressure and the composition of the fluids (Batzel and Wang, 1992). Below we present the procedure used to calculate the gases (mixture of methane and CO_2) and brine properties.

Gas

The specific gravity, G, defines a gas or a mixture of gases and it has values between 0.56 and 1.8. The specific gravity is calculated by dividing the density of the gas or mixture of gases by the density of the air at 1atm and 15.6°C. An approximation of the specific gravity of the gas will be enough to make a good estimate of its properties (Batzel and Wang, 1992).

To calculate the properties of the gas, it was necessary to estimate the pseudo-reduced temperature and pressure using the following equations:

$$P_{pr} = \frac{P}{(4.892 - 0.4048G)} \tag{3}$$

$$T_{pr} = \frac{T_a}{(94.72 + 170.75G)} \tag{4}$$

where P_{pr} and T_{pr} are the pseudo-reduced pressure and temperature respectively, P is the pressure (in MPa), G is specific gravity and T_a is the absolute temperature defined by equation 5.

$$T_a = T + 273.15 \tag{5}$$

where T is the temperature in Celsius.

The density of the gas is determined using equation 6 which depends on the pressure P, specific gravity G, the compressibility factor Z, the gas constant R, and the absolute temperature T_a.

$$\rho \cong \frac{28.8 \cdot G \cdot P}{Z \cdot R \cdot T_a} \tag{6}$$

Equation 7 and 8 were used to calculate the compressibility factor Z in terms of the pseudo-reduced temperature and pressure.

$$Z = \left[0.03 + 0.00527\left(3.5 - T_{pr}\right)^3\right] P_{pr} + \left(0.642T_{pr} - 0.007T_{pr}^4 - 0.52\right) + E \tag{7}$$

$$E = 0.109\left(3.85 - T_{pr}\right)^2 e^{\left\{-\left[0.45 + 8\left(0.56 - \frac{1}{T_{pr}}\right)^2\right]\frac{P_{pr}^{1.2}}{T_{pr}}\right\}} \tag{8}$$

The bulk modulus K_s for adiabatic conditions was estimated according to:

$$K_s = \frac{P}{\left(1-\frac{P_{pr}}{Z}\cdot\frac{\partial Z}{\partial P_{pr}}\right)_T}\,\gamma_0; \qquad (9)$$

where the derivative $\partial Z/\partial P_{pr}$ is calculated from equation 7 and 8 and γ_0 with equation 10:

$$\gamma_0 = 0.85 + \frac{5.6}{(P_{pr}+2)} + \frac{27.1}{(P_{pr}+3.5)^2} - 8.7\,e^{[-0.65(P_{pr}+1)]}. \qquad (10)$$

These equations are good approximations for the conditions that we usually find in exploration (Batzel and Wang, 1992).

Brine

Using empirical data, a relationship to estimate the density of sodium chloride solutions was developed. This relationship establishes a dependence of the density on the pressure and temperature conditions, as well as on the salinity as follows:

$$\rho_w = 1 + 1\cdot 10^{-6}(-80T - 3.3T^2 + 0.00175T^3 + B), \qquad (11a)$$

$$B = 489P - 2TP + 0.016T^2P - 1.3\cdot 10^{-5}T^3P - 0.333P^2 - 0.002TP^2, \qquad (11b)$$

$$\rho_B = \rho_w + S\{0.668 + 0.44S + 1\cdot 10^{-6}C\}, \qquad (12a)$$

$$C = 300P - 2400PS + T(80 + 3T - 3300S - 13P + 47PS), \qquad (12b)$$

where ρ_w is the water density, ρ_b is the brine density and S is the salinity in ppm/1000000. Equation 12 is adequate only for sodium chloride solutions (Batzel and Wang, 1992).

The estimation of the water velocity V_w was calculated using equation 13 which can be used for pressure and temperature conditions up to 100MPa and 100°C respectively.

$$V_w = \sum_{i=0}^{4}\sum_{j=0}^{3} w_{ij}T^iP^j \qquad (13)$$

where wij are the constants provided in table 4.

Table 4. Constants for water velocity calculation (From Batzel and Wang, 1992).

Coefficient	Value	Coefficient	Value	Coefficient	Value
w_{00}	1402.85	w_{21}	2.747×10^{-4}	w_{42}	5.230×10^{-11}
w_{10}	4.871	w_{31}	-6.503×10^{-7}	w_{03}	-1.197×10^{-5}
w_{20}	-0.04783	w_{41}	7.987×10^{-10}	w_{13}	-1.628×10^{-6}
w_{30}	1.487×10^{-4}	w_{02}	3.437×10^{-3}	w_{23}	1.237×10^{-8}
w_{40}	-2.197×10^{-7}	w_{12}	1.739×10^{-4}	w_{33}	1.327×10^{-10}
w_{01}	1.524	w_{22}	-2.135×10^{-6}	w_{43}	-4.614×10^{13}
w_{11}	-0.0111	w_{32}	-1.455×10^{-8}	----	----

In order to calculate the velocity of the brine V_b, the salinity effect was included in equation 14 (Batzel and Wang, 1992).

$$V_b = V_w + S \cdot D + S^{1.5}(780 - 10P + 0.16P^2) - 820S^2 \quad (14a)$$

$$D = (1170 - 9.6T + 0.55T^2 - 8.5 \cdot 10^{-5}T^3 + 2.6P - 0.0029TP - 0.0476P^2) \quad (14b)$$

Table 5 present the data used in this study for the calculation of the fluid properties.

Table 5. Data used for gas properties calculation

Property	Value
Methane Specific Gravity	0.5537
CO_2 Specific gravity	1.5189
Reservoir temperature	41.66 °C
Salinity	8000ppm

Gassmann Fluid Substitution

Using the values of V_p, V_s and density selected from the well log data available in the area of study (Table 3), we determined the bulk modulus of the saturated rock for the initial condition, in our case 100% brine saturated coal, according to:

$$K_{sat} = \rho_b \left(V_p^2 - \frac{4}{3} V_s^2\right), \quad (15)$$

which is defined in terms of the bulk density ρ_b, the compressional wave velocity V_p and the shear wave velocity V_s (Kumar, 2006). The shear modulus G, will be constant during the fluid substitution process and is calculated according to: (Smith et al., 2003).

$$G = \rho_b V_s^2. \quad (16)$$

In order to estimate the bulk modulus of the frame of the rock or the dry rock, K*, we used the results presented by Yu et al. (1993). In their paper, after performing laboratory tests, they conclude that the bulk modulus of the dry rock corresponds to approximately 15% less than the bulk modulus of the same rock saturated with water (Yu et al., 1993), so that:

$$K^* = 0.85K_{sat}. \quad (17)$$

The calculation of the bulk modulus of the mineral matrix is more complicated since the standard procedures are not applicable for coals. In order to estimate an appropriate value for our area of study, we decided to evaluate possible values for K_o, using limit values of V_p, V_s and density associated with coals. To do this, we graph the variation of the bulk modulus of the mineral matrix with the porosity and a parameter epsilon defined as:

$$K^* = \varepsilon\, K_{sat} \tag{18}$$

The bulk modulus of the mineral matrix was calculated using equation18 and 19:

$$K^* = \frac{K_{sat}\left(\frac{\phi K_0}{K_{fl}} + 1 - \phi\right) - K_0}{\frac{\phi K_0}{K_{fl}} + \frac{K_{sat}}{K_0} - 1 - \phi}\ , \tag{19}$$

where K_{fl} is the bulk modulus of the fluids in the pore space, and ϕ is the porosity (Smith et al., 2003). For these calculations, epsilon varies between 0.6 and 0.9 and the porosity is in the range of 0.001-6%.

Figure 5 present the variation of K_o with respect to ε and the porosity for maximum and minimum V_p associated with coals.

Figure 5a, corresponds to the variation of K_o calculated using a V_p value of 3048m/s. In this case, K_o does not present major variations for ε between 0.6 and 0.9 and porosities of 0.1 and 4%. For the higher porosities (4%-6%), K_o becomes bigger as ε decrease. From this graph, K_o tends to slowly increase from 14 to 18GPa with the increase of the porosity.

Figure 5b corresponds to the variation of K_o calculated using a V_p value of 2177m/s. In this case, K_o does not present representative variations when changing ε from 0.6 to 0.9. In terms of the effects of the porosity, the variation of K_o is not significative for the range of porosity evaluated, presenting values in the range of 1.54-1.59GPa.

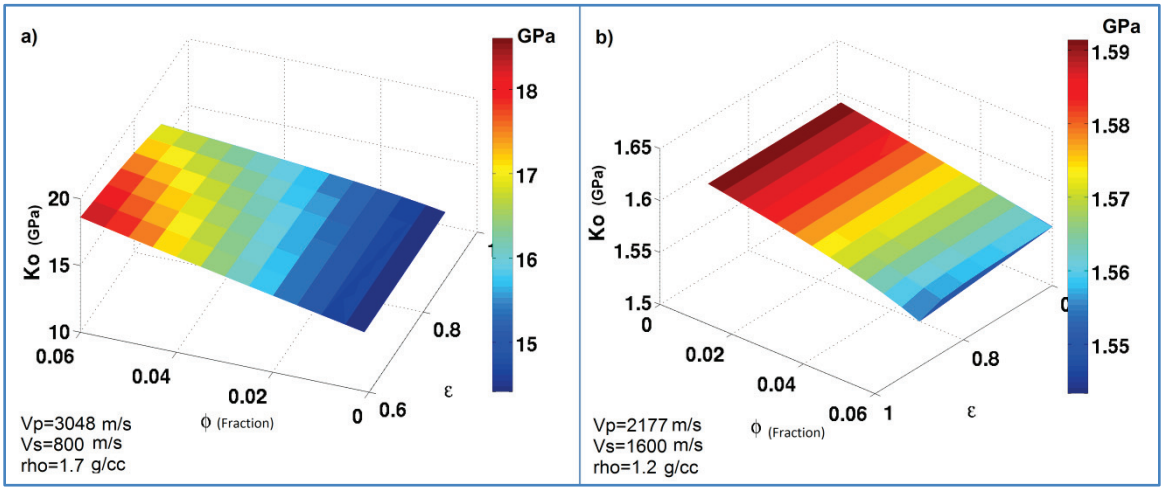

FIG. 5. Dependence of the mineral matrix bulk modulus with ε and the porosity ϕ a) Using maximum V_p value associated with coals and b) using minimum V_p value associated with coals.

Figure 6a shows the ε, ϕ, K_o surface, calculated using the values of V_p, V_s and density in Table 3, which correspond to the values selected for our area of study in the San Juan Basin. As we can see this surface behaves similar to the surface calculated using the maximum V_p value for coals and in this case, K_o varies in the range of 6.98-7.77GPa. Figure 6b present the three surfaces together.

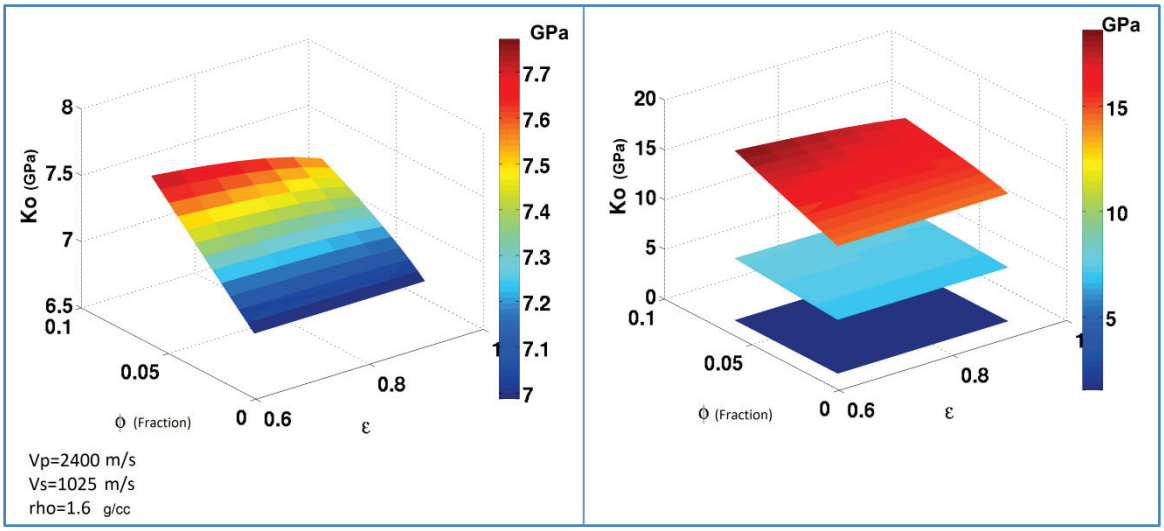

FIG. 6. Dependence of the mineral matrix bulk modulus with ε and the porosity ϕ a) Using V_p, V_s and density values associated with the San Juan Basin b) Comparison of the three surfaces (maximum V_p, minimum V_p, San Juan Basin data)

The K_o value for this study was selected from the surface presented in Figure 6a, taking into account the values that correspond to a porosity in the range of 0.1-1% and an ε between 0.8 and 0.9. The selected value for K_o is 7.04GPa.

Based on the results of the fluid simulation, which provided us the water, methane and CO_2 saturation, the density of this mix of fluids is calculated according to equation 20:

$$\rho_{flmix} = \phi_{CH_4}\,\rho_{CH_4} + \phi_{brine}\,\rho_{brine} + \phi_{CO_2}\,\rho_{CO_2} \qquad (20)$$

where ρ_{CH4}, ρ_{brine} and ρ_{CO2} are the methane, brine and CO_2 density respectively, and ϕ_{CH4}, ϕ_{brine} and ϕ_{CO2} are the volume fraction of each component (Batzel and Wang, 1992). The bulk modulus for this mix of fluids was calculated according to:

$$\frac{1}{K_{flnew}} = \frac{\phi_{CH_4}}{K_{CH_4}} + \frac{\phi_{brine}}{K_{brine}} + \frac{\phi_{CO_2}}{K_{CO_2}} \qquad (21)$$

where K_{CH4}, K_{brine} and K_{CO2} and K_{brine} are the bulk modulus of the CH_4, brine and CO_2 (Batzle and Wang, 1992) previously calculated using Batzel and Wang equations (1992).

Using the bulk modulus calculated for the mix of methane, brine and CO_2, we use equation 19 to estimate the bulk modulus of the rock saturated with this mix of fluids (Smith et al., 2003).

The new bulk density of the rock, ρ_{new} , after the fluid substitution, is calculated according to:

$$\rho_{bnew} = \rho_g(1-\phi) + \rho_{flmix}\phi, \qquad (22)$$

where ρ_g is the matrix density (Smith et al., 2003). Finally the velocity of the compressional and shear waves is estimated with equation 15 and 16 using the bulk modulus of the rock, saturated with the new fluid (Smith et al., 2003).

Again, the applicability of the Gassmann equation is based on assumptions about the structure and pore space of the rock. We use the Gassmann equation in coals based on the fact that the matrix porosity present low permeability and that the macroporosity system (cleats) is the one that controls the fluid flow. For this study, we assume that the fluid substitution is performed taking into account only effective porosity.

RESULTS

Fluid simulation

The fluid simulation provides us with data of methane, CO_2 and water saturation, pressure, and CO_2 and methane concentration from 2002 until 2031. In this report we present the methane, CO_2 and water saturation for 2002, representing the case of the field after several years of depletion; 2005 after 2 years of CO_2 injection; and 2011, 1 year after shutting the injection wells.

Figure 7a show a high saturation of methane over the complete area of study, more specifically around 80% of methane saturation. Figure 7b presents the CO_2 saturation. The presence of CO_2 in the area is also homogeneously distributed and present values around 18-20%. Figure 7c represents a coalbed that has been dewatered and presents water saturation in the order of 10^{-2}%. The water saturation at this stage tends to increase from SW to NE.

Figure 8 shows fluid saturations after 2 years of injection of CO_2 into the coalbed. In Figure 8a, it is possible to appreciate a decrease in the methane saturation around the injector wells. In the zones surrounding the injectors well it is possible to identify the footprint of the CO_2 injection with a radial distribution. In these zones, there is a reduction of the methane saturation from 80% (in 2002) to less than 15%. Figure 8b presents the increase of CO_2 saturation in the vicinities of the injector wells. An increase of the CO_2 saturation from 20% to 85% or more is observed. The water saturation also has been affected by the CO_2 injection; it is possible to appreciate the footprint created by the displacement of water due to CO_2 injection. Along the rest of the area of study the water saturation seams to keep the same trend.

One year after finishing the CO_2 injection, the CO_2 flood is still evident in the saturation maps. The area affected by the CO_2 injection has expanded through the years. In these zones the CO_2 saturation remains in the order of 90% and the methane saturation close to 10% (Figure 9a and 9b). The distribution of the CO_2 flood around the injector well does not present a radial distribution anymore and it seems to be displacing to the South where lower pressures are dominant. The water saturation continuously decreases specially in the areas surrounding the injector wells.

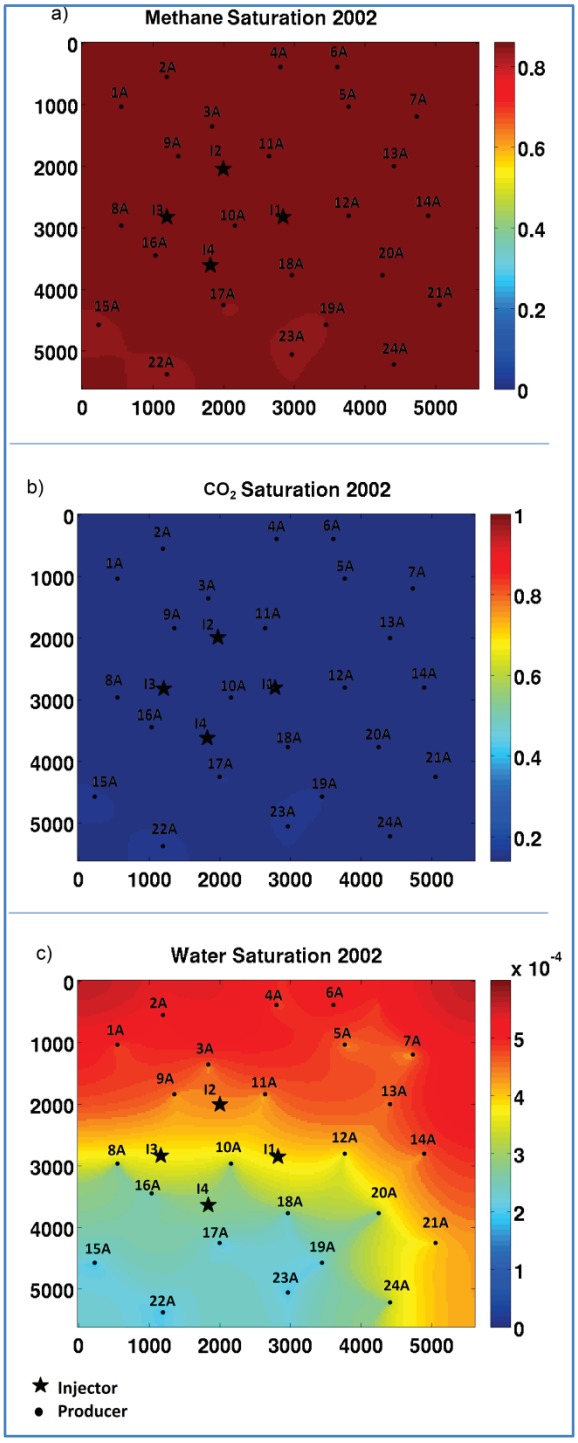

FIG. 7. a) Methane, b) CO_2 and c) water saturation for 2002. Presents the reservoir after several years of depletion

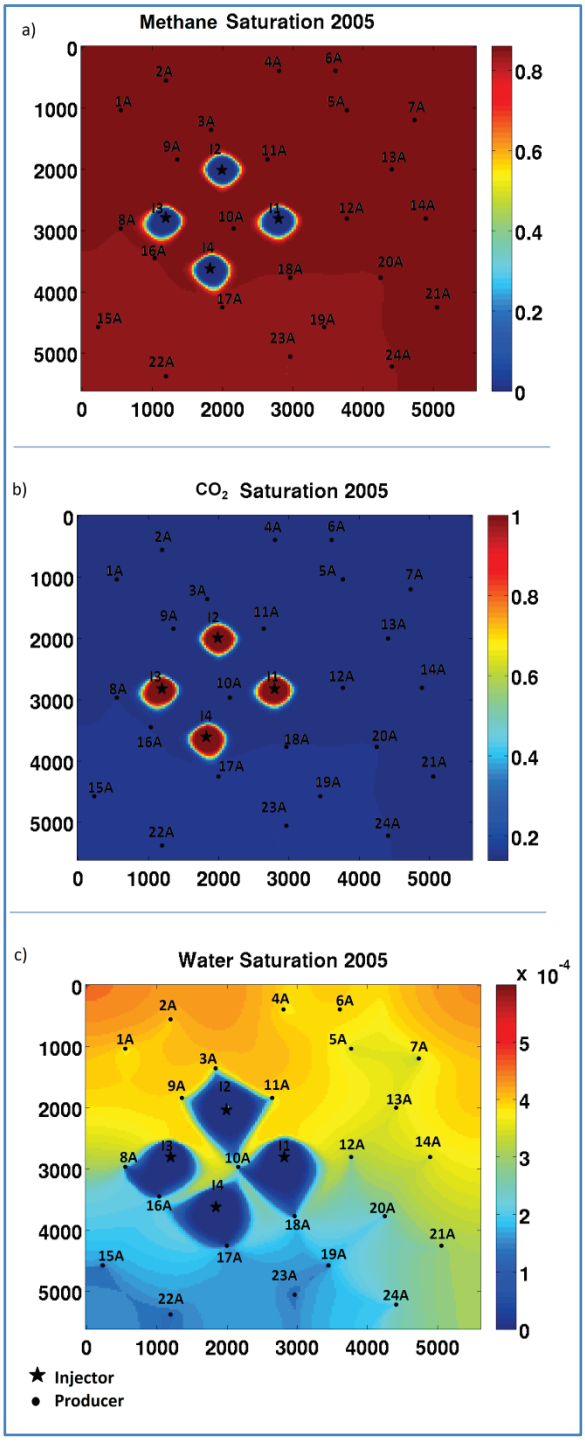

FIG. 8. a) Methane, b) CO_2 and c) water saturation for 2005. Presents the reservoir after 2 years of CO_2 injection

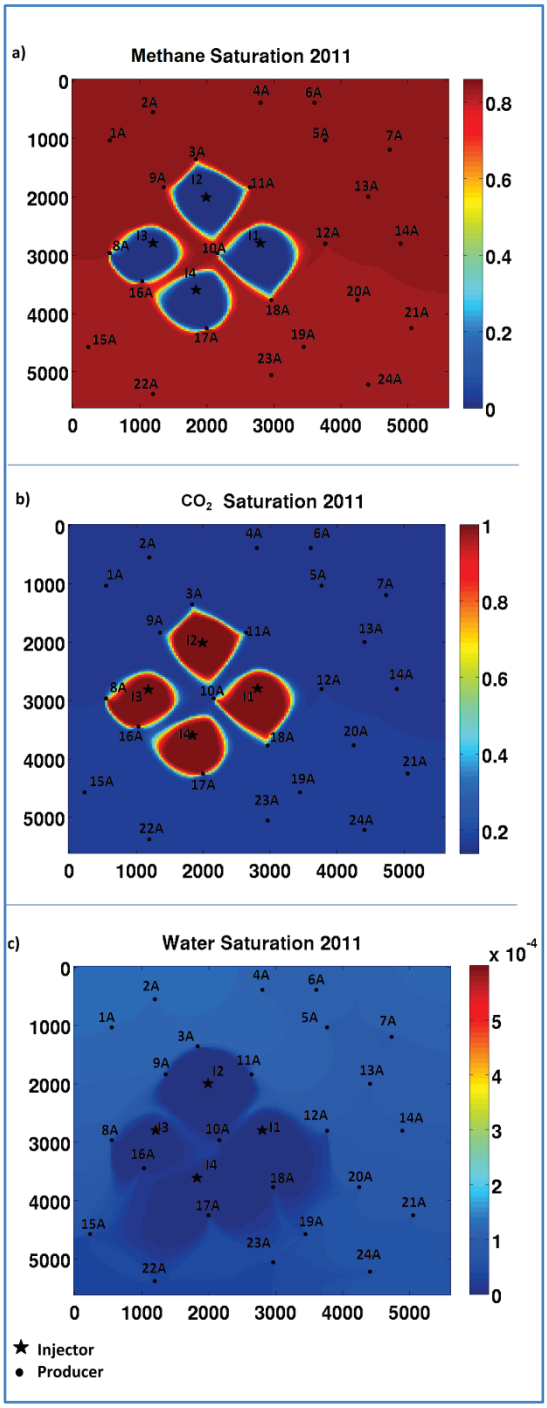

FIG. 9. a) Methane, b) CO_2 and c) water saturation for 2011. Presents the reservoir 1 year after shutting the injection wells

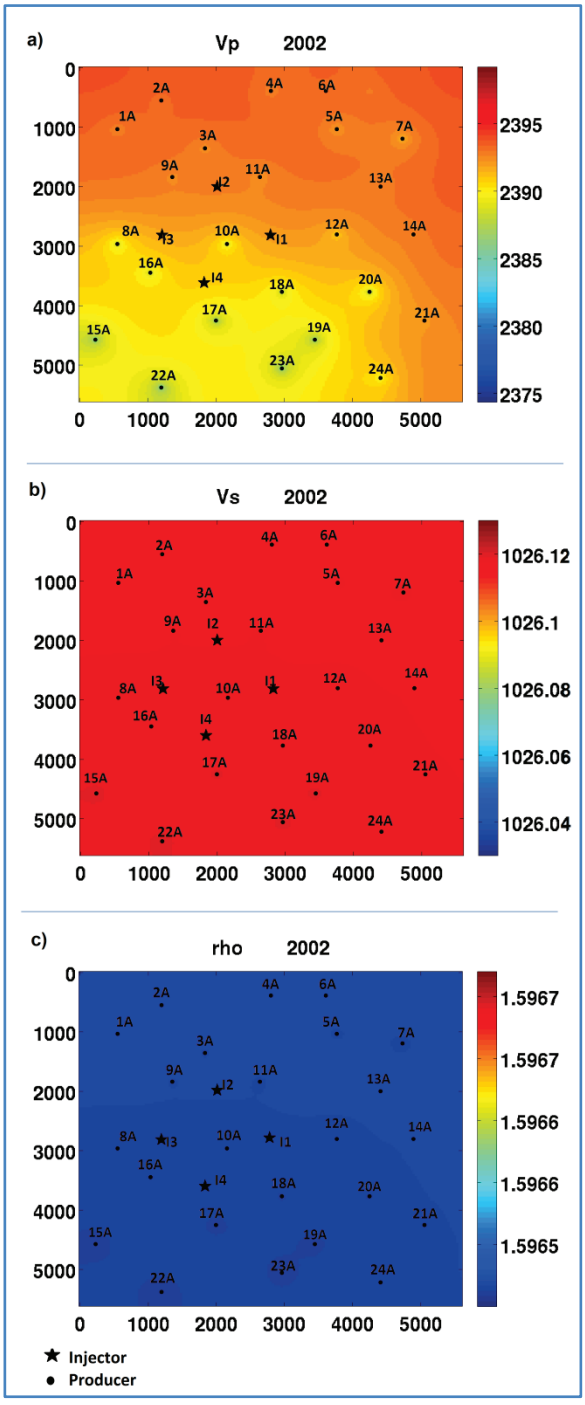

FIG. 10. a) Compressional wave velocity, b) shear wave velocity and c) density map for 2002, after several year of primary production

Fluid substitution

The Gassmann fluid substitution allows us to compare changes in compressional wave velocity, shear wave velocity and density for different fluid saturations. Here, we compare the change due to depletion and CO_2 injection in a 50ft coalbed.

As an initial state we assume that the coalbed was fully saturated with brine and the values of V_p, V_s and density for this stage are presented in Table 3.

Figure 10, 11 and 12 present the variation of V_p, V_s and density in the area of study. In the case of the compressional wave velocity, it decreased from the initial value of 2450m/s to a range of 2390-2395m/s when replacing brine by methane in the pore space (Figure 10a). In the velocity map presented in Figure 10a V_p tends to slowly increase from SW to NE. After CO_2 injection we observed that, in the area around the injector wells, there is an area of lower velocity associated with the increase of CO_2 saturation in that zone of coalbed (Figure 8b and 11a). After shutting injector wells the CO_2 flood seems to be moving to the South, where the area presents the lower pressures, and this is also evident in the velocity map in Figure 12a. In this case, we observed a decrease in V_p along the complete area of study that can be associated to depletion. The lowest velocities are in the South of the area of study and this can be related to a decrease in the methane saturation and lower pressures in this zone (Figure 12a and Figure 9a).

The shear wave velocity has a more homogeneous distribution than the compressional wave velocity (Figure 10a and 10b). After replacing brine by methane, the change in the shear wave velocity is not relevant. The footprint of CO_2 injection in the coalbed is also evident in the shear wave velocity map but the magnitudes of the changes are not representative (Figure 11b and 12b). The bulk density presents a similar behavior to the shear wave velocity and the magnitudes of the density changes are not meaningful as well (Figure 11c and 12c).

Impedance analysis

We use Elastic Impedance and Elastic Impedance Coefficient to attempt to discriminate methane from CO_2 in a coalbed.

Figure 13 presents the elastic Impedance and the Elastic Impedance Coefficient for the area of study before the CO_2 injection started (2002). Figure 13a show a decrease of the Elastic Impedance from South to North and along the area of study we can appreciate peaks of low Elastic Impedance. These peaks of low Elastic Impedance are associated to the location of the 24 wells in the area of study. The decrease of the elastic Impedance in the areas surrounding each well is consequence of the decrease of the compressional wave velocity in that area due to reduction of pressure. The wells located in the northern part of the area of study produce a stronger response where the highest pressures are present. Figure 13b shows the response of the Elastic Impedance Coefficient of the Fruitland coals in the area of study. The result is similar to the one obtained with the Elastic Impedance with a tendency to increase from South to North.

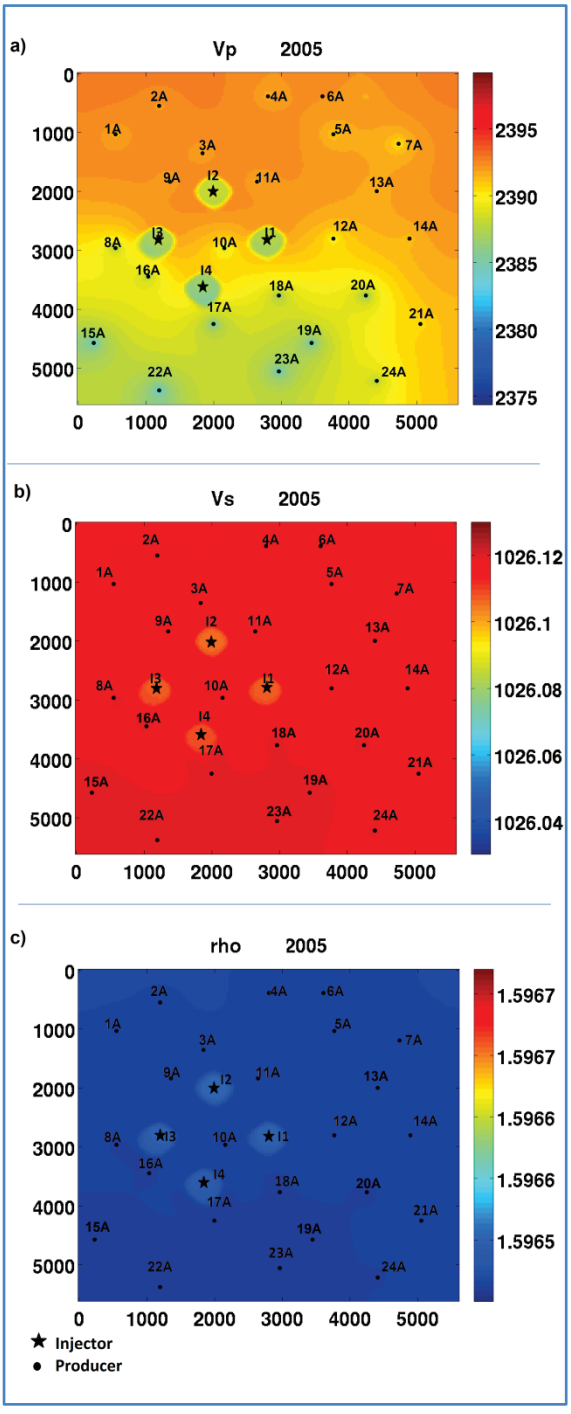

FIG. 11. a) Compressional wave velocity, b) shear wave velocity and c) density map for 2005, after 2 year of CO_2 enhanced coalbed methane production

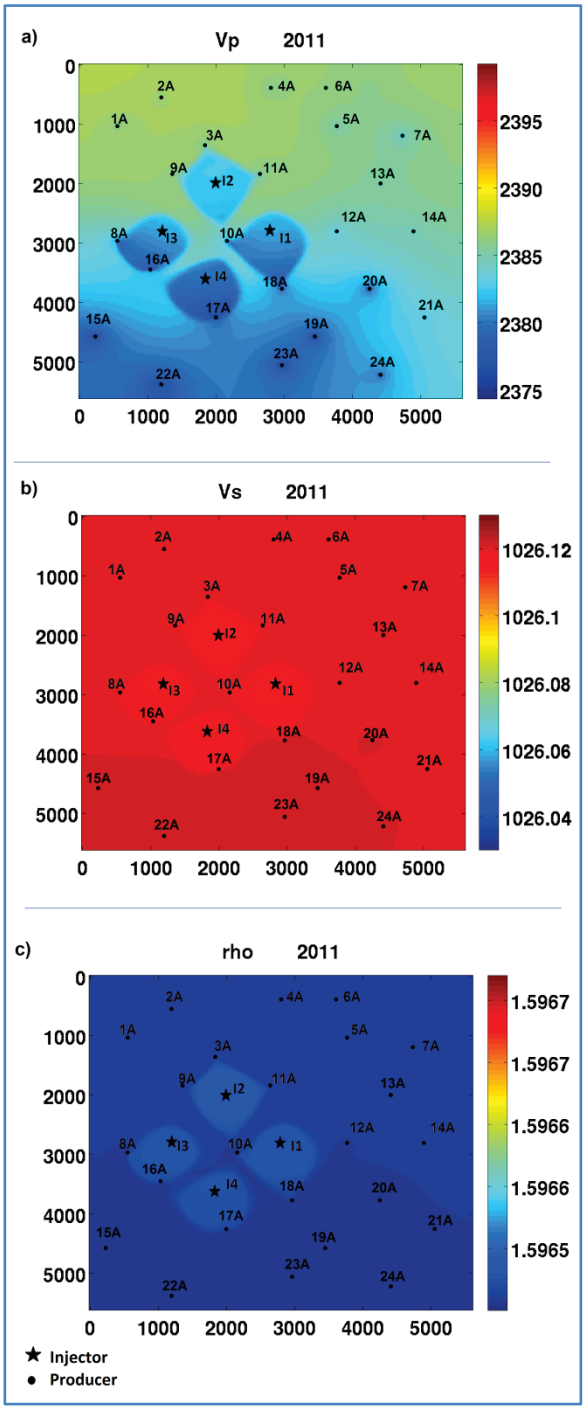

FIG. 12. a) Compressional wave velocity, b) shear wave velocity and c) density map for 2011, 1 year after shutting the injector wells

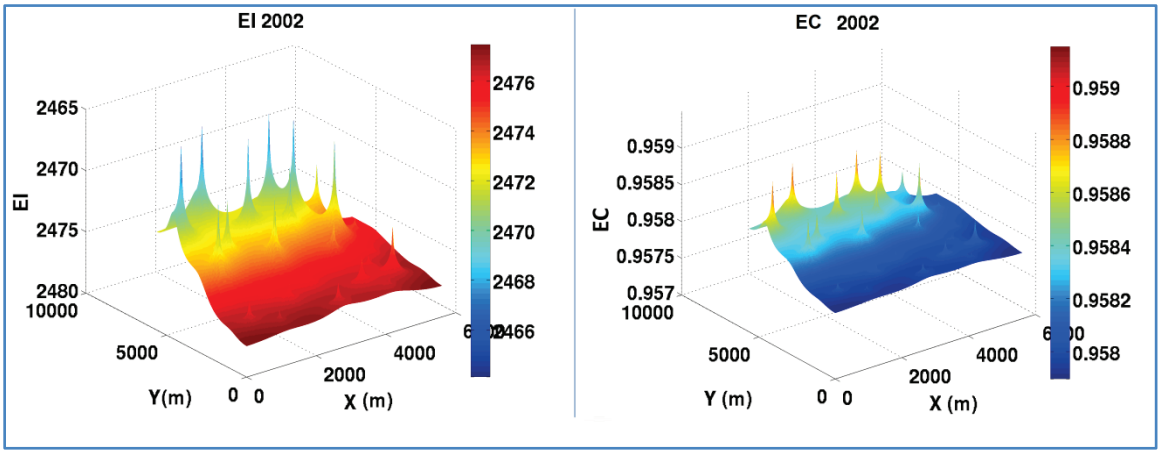

FIG. 13. a) Elastic Impedance and b) Elastic Impedance Coefficient response before CO_2 injection

Figure 14 shows the EI and the EC response two years after starting CO_2 injection. In Figure 14a we can still observe the low EI response in the vicinity of the well locations and that the EI tends to decrease from South to North. In this case, it is also possible to observe the path of the flood of CO_2 that has been injected. In the area inside the red circle, there are four zones of low EI that corresponds to the vicinities of the injector wells and the areas of higher CO_2 saturation in that period of time (2005). In the exact location of the four injector wells, there is a local high in the EI response that could be associated to the changes in the pressure due to injection (Figure 14a).

Figure 14b presents the EC response. The red circle delineates the area affected by CO_2 injection and the EC high response associated with the CO_2 flood. Similar results to the EI can be observed with EC but with less detail. The EC seems to delineate better the changes that are consequence of CO_2 injection, and in this case it does not show the response associated to the changes in pressure due to injection in the injector wells location (local high of Elastic Impedance in Figure 14a)

The changes in Elastic Impedance and Elastic Impedance Coefficient that we observe in the area of study allow us to monitor the movement of the CO_2 that has been injected, through the coalbed. However this attributes did not provide a good discrimination between the coalbed saturated with CO_2 and saturated with methane. In Figure 14, we can observe that the EI and EC values associated with the coalbed saturated with mostly CO_2 are also associated to some zones mostly saturated with methane.

Figure 15 show the EI an EC response of the area of study, one year after stopping CO_2 injection. In Figure 15a, the zones of injection have a low EI response and the footprint of the displacement of the CO_2 injected is evident (red circle). With the EC (Figure 15b), the effects of the CO_2 injection seems to be the most relevant changes in the area of study, presenting higher values of EC than the surrounding areas.

In this case (Figure 15) EC highlight more the CO_2 footprint than the EI, in which the effects due to CO_2 injection have the same relevance that the effect of pressure variation around the producer wells location.

The changes in EI an EC in Figure 14 and 15 are small in magnitude and it is difficult to predict if it will be possible to identify the CO_2 front in seismic.

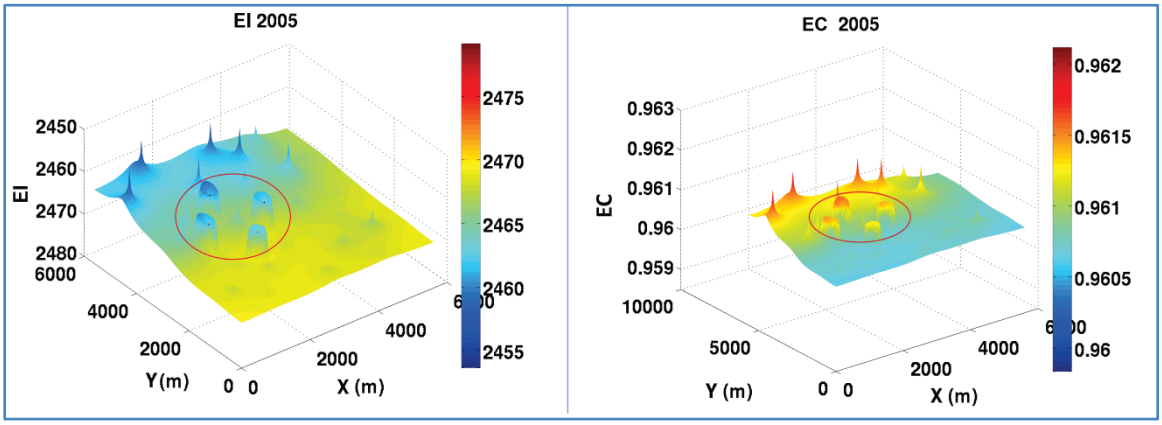

FIG. 14. a) Elastic Impedance and b) Elastic Impedance Coefficient response two years after starting CO_2 injection

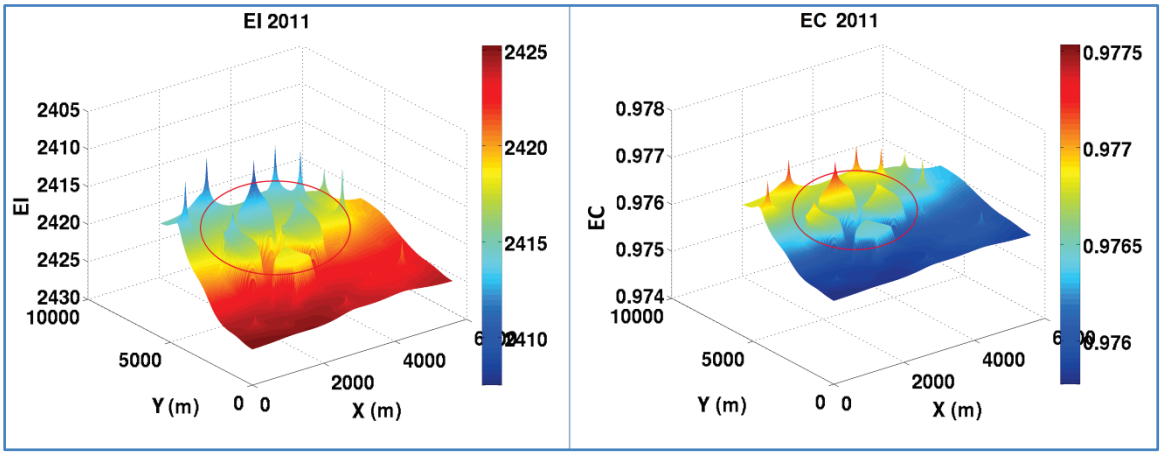

FIG. 15. a) Elastic Impedance and b) Elastic Impedance Coefficient response one year after shutting the injector wells

CONCLUSIONS

The fluid simulation gave us important information about the distribution of CO_2, methane and brine in the area of study as well as of the saturation of each of them. The fluid simulation provided the data required to perform the fluid substitution and estimate changes in V_p, V_s and density, associated with coalbed methane primary production and enhanced coalbed methane by CO_2 injection.

The changes in V_p obtained from the Gassmann fluid substitution, after replacing brine by methane, were a decrease around 55m/s for the primary production case and around 65m/s by 2011, after finishing CO_2 injection. The movement of the CO_2 flood can be appreciated in the velocity maps and it is associated to a decrease in V_p.

In the case of the V_s and density, it is possible to identify the CO_2 flood but in this case, the changes present a small magnitude and are not representative.

Attributes like Elastic Impedance and Elastic Impedance Coefficient, were used as tools to attempt the discrimination of CO_2 and methane saturated coalbeds, as well as the monitoring of the CO_2 injected flood. In this case, Elastic Impedance and Elastic Impedance Coefficient were not able to completely differentiate the presence of CO_2 and methane but it was possible to monitor the movement of the CO_2 flood during and after injection. The changes due to CO_2 injection were evident in EI and EC but the last one tends to highlight the CO_2 effect over the other changes in impedance in the area.

The changes in EI an EC that were appreciated are small and it was difficult to determine if these changes are going to be evident in seismic.

ACKNOWLEDMENT

The authors want to thank the Consortium for Research in Elastic Wave Exploration Seismology (CREWES) and the Natural Science and Engineering Research Council of Canada (NSERC, CRDPJ379744-08) for supporting this project. We also want to thank Faranak Mahmoudian, Mahdi Almutlaq, CREWES sponsors, staff and students.

REFERENCES

Batzle M. and Wang Z. 1992. Seismic properties of pore fluids. Geophysics 57, 1396-1408.

Cao H., Yang Z., and Li Y. Elastic Impedance Coefficient (EC) for Lithology Discrimination and Gas Detection. SEG Las Vegas Annual Meeting, SGA001526

Connolly P. 1999. Elastic Impedance. The Leading Edge 18, 438-452

Crist T.E., Boyer C.M., and Kelso B.S. 1989. A Geologic and Coalbed Methane Resource Analysis of the Menefee Formation in the San Juan Basin, Southwestern Colorado and Northwestern New Mexico. Low Permeability Reservoirs Symposium, 00018945-MS

Jenkins C., DeGolyer, MacNaughton, and Boyer C. 2008. Coalbed and Shale Gas Reservoirs. Journal of Petroleum Technology 60, 92-99

Jones A., Ahmed U., Bush D., Holland M., Kelkar S.M., Rakop K.C., Bowman K.C., and Bell G.J. 1984. Methane Production Characterization for a Deeply Buried Coalbed Reservoir in the San Juan Basin. Unconventional Gas Recovery Symposium, SPE/DOE/GRI 12876

Jordan J., Harkrider J. Anthony W., DeLong T., and Martin R. 2003. The relationship Between Net Pressure Development During Hydraulic Fracture Treatments and Productivity in Fruitland Coal Completions. SPE Eastern Regional Meeting, 00084819-MS

Kaiser W.R., and Ayers W.B. 1994. Geologic and Hydrologic Characterization of Coalbed Methane Reservoirs in the San Juan Basin. SPE Formation Evaluation 9, 175-184

Koperna G., Oudinot A., McColpin G., Liu N., Heath J., Wells A., and Young G. 2009. CO_2-ECBM/Storage Activities at the San Juan Basin's Pump Canyon Test Site. SPE Annual Technical Conference and Exhibition, SPE 124002

Kumar D. 2006. A tutorial on Gassmann Fluid Substitution: Formulation, Algorithm and Matlab Code. Geohorizons 11, 4-12.

Laubach S.E., and Tremain C.M. 1991. Regional coal fracture patterns and coalbed methane development. The 32nd U.S. Symposium on Rock Mechanics (USRMS), ISBN 90 6191 194X

Magill D., Ramurthy M., Jordan J., and Nguyen P. 2010. Controlling Coal-Fines Production in Massively Cavitated Openhole Coalbed-Methane Wells. SPE Asia Pacific Oil and Gas Conference and Exhibition, SPE 134031-MS

Michael E., Anders D., and Law B. 1993. Geochemical evaluation of Upper Cretaceous Fruitland Formation coals, San Juan Basin, New Mexico and Colorado. Organic Geochemestry 20, 475-498

Oudinot A., Koperna G., Philip Z., Liu N., Heath J., Wells A., Young G., and Wilson T. 2009. CO_2 Injection Performance in the Fruitland Coal Fairway, San Juan Basin: Results of a Field Pilot. SPE International Conference on CO_2 Capture, Storage, and Utilization, SPE 127073-MS

Pashin, J. 1998. Stratigraphy and structure of coalbed methane reservoirs in the United States: An overview. International Journal of Coal Geology 35, 209-240

Ramos A., and Davis T. 1997. 3-D AVO analysis and modeling applied to fracture detection in coalbed methane reservoirs. Geophysics 62, 1683-1695

Ramurthy M., and Lyons B. 2007. Lessons Learned From Modeling Hydraulic Fracture Treatments in Coals Using a Fully Functional Three-Dimensional Fracture Model in a San Juan Basin Project. Rocky Mountain Oil & Gas Technology Symposium, SPE 107972

Smith T., Sondergeld C. and Rai C. 2003. Gassmann fluid substitution: A tutorial. Geophysics 68, 430-440

Snyder G., Riese W., Franks S., Fehn U., Pelzmann W., Gorody A., and Moran J. 2003. Origin and history of waters associated with coalbed methane: 129I, 36Cl, and stable isotope results from the Fruitland Formation, CO and NM. Geochimica et Cosmochimica Acta 67, 4529-4544

Whitcombe D. 2002. Elastic Impedance normalization. Geophysics 67, 60-62

Young G.B.C., McElhiney J.E. and Paul G.W. 1991. An Analysis of Fruitland Coalbed Methane Production, Cedar Hill Field, Northern San Juan Basin. SPE Annual Technical Conference and Exhibition, 00022913-MS

Yu G., Keeva V., and Durney D. 1993.The influence of confining pressure and water saturation on dynamic elastic properties of some Permian coals. Geophysics 58, 30-38

Zarantonello S., Bevc D. and Harris J. 2010.integrated reservoir, petrophysical, and seismic simulation of CO2 storage in coal beds. The Leading Edge 29, 184-190.